Proceedings of the ASME 2010 3rd Joint US-European Fluids Engineering Summer Meeting and 8th International Conference on Nanochannels, Microchannels, and Minichannels
FEDSM-ICNMM2010
August 1-5, 2010, Montreal, Canada

FEDSM-ICNMM2010-30906

VISUALIZING PRINCIPAL MESH MODIFICATION ACTIONS ACCORDING TO AN INTERPOLATION ERROR BASED ESTIMATOR ON THE DIFFUSER

Paul Labbé*
Institut de recherches d'Hydro-Québec
1800 boul. Lionel-Boulet,
Varennes(Québec), H3X 1X1, Canada
Tel: 450-652-8362, Fax: 530-752-4158
Email: labbe.paul@ireq.ca, WWW: http://www.ireq.ca

François Guibault
Department or Computer and Software Engineering
École Polytechnique de Montréal
2900, boul. Édouard-Montpetit, Campus de l'Université de Montréal,
Montréal (Québec), H3T 1J4, Canada,
514-340-4711 x4876
francois.guibault@polymtl.ca, WWW http://www.polymtl.ca

ABSTRACT

Anisotropic mesh adaptation offers a methodology that iteratively marches towards a mesh that equidistributes the interpolation error of scalars. In order to quantify potential improvements to a mesh that can be brought by mesh adaptation, a novel mesh descriptor and associated visualization tool are presented. The combination of the mesh descriptor, which is based on interpolation error estimation, and the associated visualization approach, aims to provide CFD analysts with a quantitative tool to guide manual or automatic mesh adaptation. The experiment of Clausen on the swirling boundary layer in a conical diffuser is used as a real world test case to assess the potential of the approach.

NOMENCLATURE

ρ, μ, β', α_1, α_2, β_1, β_2,
$\sigma_{\omega 1}$,$\sigma_{\omega 2}$, σ_{k1}, σ_{k2} Constants of the model.
$\mathscr{T}$ The mesh.
K An element of the mesh.
M_k Metric of element K.
u Exact solution to a PDE.
u_h Approximate solution to a PDE.
$\Pi_h(u)$ Interpolation of u on $\mathscr{T}$.
$H(u)$ Hessien of u.
$\tilde{H}(u)$ Reconstructed Hessien of u.
M_s Target metric.
$\mathscr{E}_K$ Non conformity of element K.

INTRODUCTION

Swirling flows have been extensively studied in the past [1–5], and two general flow configurations can be considered. The first flow configuration is composed of swirling jets, which are of great interest to study geophysical and aerodynamics flows, and for instance tip vortices produced over wings. Tip vortices are typically characterized by a purely axial flow superimposed upon the rotational motion of the jet. Depending on the orientation and the amplitude of the axial flow velocity, many flow applications can be characterized. The second flow configuration comprises swirling flows developing in a confined area. In this case, the entire inlet flow field exhibits a rotational motion. Its downstream development depends on the interaction with boundaries. In general, these flow configurations have a finite aspect ratio, so that the outlet boundaries exert a direct influence on the entire flow structure. Such devices are for example found in chemical processes and food industries to separate gas bubbles from a liquid. In the case of hydraulic turbines, the flow downstream of the runner exhibits properties of both cat-

*Address all correspondence to this author.

egories [6]. Indeed, the flow undergoes a solid body rotation confined by a conical surface, which highlights the importance of the axial flow on the flow stability.

In order to accurately capture swirling flow behavior in a hydraulic turbine draft-tube cone through numerical simulations, two main challenges remain. The first relates to the precise modeling of turbulence, especially in the presence of instabilities and detached vortices, as observed in draft-tubes at part-load or overload points of operation. The second challenge has to do with the adequate spatial discretization of the computational domain through correct mesh sizing and element shape control.

While anisotropic mesh adaptation has been extensively used to improve simulation predictions for external aerodynamic configurations [7–9], much less work has been devoted to the accurate capture of internal flow configurations involving vortices and swirl. Recent work by Joubarne et al. [10] has shown how an anisotropic mesh adaptation method can significantly improve the capture of a tip vortex, however, as described above, the flow inside a turbine draft-tube is more complex, as it strongly interacts with the boundaries. The present paper aims to assess the capacity of an anisotropic mesh descriptor derived from interpolation error estimation, to help CFD analysts assess regions in the flow domain where the mesh needs to be adapted, either manually or though automatic mesh adaptation.

The experiment of Clausen [11] on the swirling boundary layer in a conical diffuser is used as a test case to verify and validate the mesh descriptor and associated visualization approach. This is seen as a first step needed to take ownership of the new adaptation technologies.

In the first part of the paper, the SST model of the RANS formulation is solved on a set of finer and finer hexahedral meshes in order to assess the grid convergence index on a very fine grid using the geometry of the ERCOFTAC conical diffuser test case. Numerical and experimental results are then compared.

In the second part of the paper, a novel mesh descriptor called the non-conformity coefficient is presented. This descriptor, based on interpolation error estimation of a solution, allows to quantify discrepancies both in shape and size of mesh elements with respect to a given solution. The solution in the conical diffuser is used as a test case to explore the potential of the non-conformity coefficient in providing analysts with valuable a posteriori information regarding mesh quality even though the simulation could be improved by correctly adjusting the parameters of the model. Indeed, we are focusing on a strategy that can help see how the error estimator evaluates the mesh, and visualize the principal operations that it wants to perform on the mesh. In this context, the numerical results need only be representative of what an actual user would do.

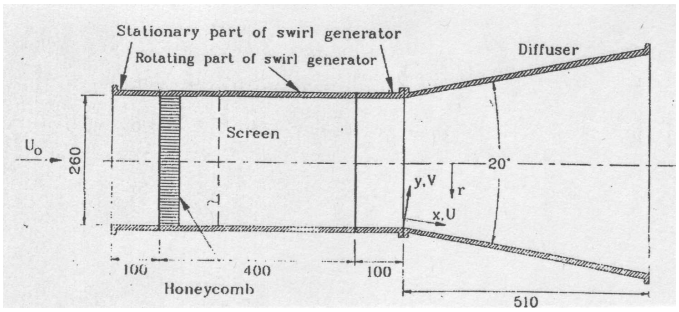

FIGURE 1. Experimental diffuser geometry (from [11]).

Conical Diffuser Simulations

As described in several publications [11–16], the ERCOFTAC conical diffuser [11] is a classical test case, part of the ERCOFTAC Classic database (Case 60: Swirling Boundary Layer in Conical Diffuser), against which a number of CFD simulation results have been compared [13–15].

This geometrically simple computational domain, illustrated in Fig. 1, was composed, in the experimental setup, of a rotating inlet section equipped with a honeycomb screen that served as a swirl generator, followed by a diffuser section with a total opening angle of 20°. Several geometric setups have been considered for the outlet section in [17]. The present simulations have been performed using a straight cylindrical extension to the domain, which corresponds to case 1 described in [17][1].

CFD MODEL

This section presents the specifications of the CFD model which was chosen for our study. First, the choice of the SST turbulence model is detailed. Initial mesh considerations are then explained, before addressing the issues of the boundary conditions.

The SST turbulence model

Our computational model uses the low-Reynolds SST turbulence model for various reasons. As our study uses the commercial code ANSYS CFX 12, the simplest way to model turbulence is to choose among the built-in solutions. The SST model seemed the most appropriate, because it uses both $k-\omega$ (for modeling the flow near the walls) and $k-\varepsilon$ behaviors (for higher Reynolds). Moreover, the rugosity can be taken into account in the latest version of the code.

First, let us consider the steady-state incompressible isothermal Navier-Stokes equations which will be solved by ANSYS

[1] Cases are also described at: http://openfoamwiki.net/index.php/Sig_Turbomachinery_/_ERCOFTAC_conical_diffuser

CFX.

$$\rho\left(\frac{\partial \mathbf{U}}{\partial t}+\mathbf{U}\cdot\nabla\mathbf{U}\right)=-\nabla p+\mu\nabla^2\mathbf{U} \tag{1}$$

$$\nabla\cdot(\rho\mathbf{U})=0 \tag{2}$$

Before understanding why the SST turbulence model is appropriate, let us sum up its specifications. As detailed in the help files of ANSYS CFX [18], its behavior is governed by the following equations.

Near the walls, the $k-\omega$ is used [18, 19]:

$$\frac{\partial(\rho k)}{\partial t}+\nabla\cdot(\rho\mathbf{U}k)=\nabla\cdot\left[\left(\mu+\frac{\mu_t}{\sigma_{k1}}\right)\nabla k\right]+P_k-\beta'\rho k\omega \tag{3}$$

$$\frac{\partial(\rho\omega)}{\partial t}+\nabla\cdot(\rho\mathbf{U}\omega)=\nabla\cdot\left[\left(\mu+\frac{\mu_t}{\sigma_{\omega1}}\right)\nabla\omega\right] \tag{4}$$

$$+\alpha_1\frac{\omega}{k}P_k-\beta_1\rho\omega^2 \tag{5}$$

On the other hand, further from the walls, $k-\varepsilon$ is used [18]:

$$\frac{\partial(\rho k)}{\partial t}+\nabla\cdot(\rho\mathbf{U}k)=\nabla\cdot\left[\left(\mu+\frac{\mu_t}{\sigma_{k2}}\right)\nabla k\right]+P_k-\beta'\rho k\omega \tag{6}$$

$$\frac{\partial(\rho\omega)}{\partial t}+\nabla\cdot(\rho\mathbf{U}\omega)=\nabla\cdot\left[\left(\mu+\frac{\mu_t}{\sigma_{\omega2}}\right)\nabla\omega\right] \tag{7}$$

$$+2\rho\frac{1}{\sigma_{\omega2}\omega}\nabla k\nabla\omega \tag{8}$$

$$+\alpha_2\frac{\omega}{k}P_k-\beta_2\rho\omega^2 \tag{9}$$

The transition between those two models in the upper boundary layer is evaluated using the following expression:

$$\Phi_3=F\Phi_1+(1-F)\Phi_2 \tag{10}$$

Where Φ_1, Φ_2 and Φ_3 respectively stand for the coefficients of the $k-\omega$ model, the $k-\varepsilon$ model, and the SST model, and F is the blending function, given by

$$F=\tanh\left(\max\left(\frac{2\sqrt{k}}{\beta\omega y},\frac{500\nu}{y^2\omega}\right)^2\right) \tag{11}$$

where y is the distance to the nearest wall.

Moreover, the SST model also uses a limiter to the eddy viscosity:

$$\nu_t=\frac{\mu_t}{\rho}=\frac{a_1k}{\max(a_1\omega,SF_2)} \tag{12}$$

In all those equations, β', α_1, α_2, β_1, β_2, $\sigma_{\omega1}$, $\sigma_{\omega2}$, σ_{k1}, σ_{k2} are constants of the model (cf. [18, 19] for details and numerical values), while P_k is the turbulent energy production, given by

$$P_k=\mu_t\nabla\mathbf{U}\cdot\left(\nabla\mathbf{U}+\nabla\mathbf{U}^T\right)-\frac{2}{3}\nabla\cdot\mathbf{U}\left(3\mu_t\nabla\cdot\mathbf{U}+\rho k\right) \tag{13}$$

Numerical experiments were performed on a sequence of finer and finer hexahedral meshes. The coarsest mesh labeled $h1$ has 125k nodes. A finer mesh labeled $h2$ has 450k nodes. The two finest meshes are $h3$ which has 2.5M nodes and mesh $h4$ has 5M nodes. The longitudinal flow component U is compared to the experiments at station $x=25mm$, $x=60mm$ and $x=100mm$ in figure 2. These results are acceptable, and the parameters of the SST model could be adjusted to yield better agreement to the experimental measures. However, the goal of adaptivity is not to give better agreement with experimental measures. Adaptivity is a procedure that helps to attain the same precision as a fine mesh, but on a much coarser mesh. Therefore, the results presented will suffice in our study.

Error Estimation

Following the work of [20], [21], [22], [23] an error estimator based on the interpolation error is used to assess where the mesh needs to be refined and where the mesh needs to be coarsened.

$$\|u-\Pi_h u\|_{\infty,K}\leq C|\Delta^t\vec{x}\tilde{H}(u)\Delta\vec{x}| \tag{14}$$

The Hessian is approximated by a reconstruction technique similar to the superconvergent patch recovery method of Zienkiewicz and Zhu [24]. In this case, however, we locally reconstruct a paraboloid from the solution from which we can derive a Hessian following the work of Vallet.

This error estimator yields a metric space that can be used to measure the interpolation error between any points. Note however that we do not follow the geodesic when computing the error between points, but integrate the interpolation error on the straight line between the points. This does not give the true metric length between the points, but does give sufficient information for our purposes.

Target metric M_s

The target metric M_s is obtained from the error estimate presented previously. Ellipses are used in figure 3 to represent all points that are at a constant error level away from the center of the element. For display purposes, the ellipse present $1/sqrt(\lambda_i)$, since $\lambda_i = 1/h_i^2$. Isolines of the scalar used corroborate the behavior of the metric.

Metric M_k of an element of the mesh

The target metric of the element can be compared to the actual metric of the element K. Indeed, the metric M_k of element K is defined as the metric of the transformation that renders K into a unit equilateral element. Formally, the metric M_k is defined so that

$$\Delta\vec{x}^t M_k \Delta\vec{x} = 1 \tag{15}$$

for all edges of element K. This means that when the edges of K are measured with the metric M_k, they are of unit length.

Using modified Lagrangian interpolation on a reference element, we can write $\Delta\vec{x} = J(\vec{r})\Delta\vec{u}$ where $\vec{u}$ refers to the parametric space of the modified Lagrangian interpolant. This leads to

$$\Delta\vec{u}^t J^t(\vec{r}) M_k J(\vec{r}) \Delta\vec{u} = 1 \tag{16}$$

The modified Lagrange basis is chosen so that the parametric length of the edges are of unit length, meaning that $\Delta\vec{u}^t\Delta\vec{u} = 1$ for each edge of K. For example, the quadrilateral element is usually defined on the parametric space $[-1,-1]\times[1,1]$. The modified quadrilateral element is defined on $[-1/2,-1/2]\times[1/2,1/2]$ instead so that the parametric edges are of unit length. Now, if we set:

$$M_k = (J^t(\vec{r}))^{-1}(J(\vec{r}))^{-1} = (J(\vec{r})J^t(\vec{r}))^{-1} \tag{17}$$

in equation 16 then we see that the edges of the modified element will be of unit length. Thus, the modified Lagrange interpolants transform K into regular elements. There are an infinite number of other transformation that also do this, but they all have the same metric M_k. A procedure described in [25] can alternatively be used for simplices. This procedure directly solves the system of equations generated when equation 15 is written for each edge and noting that the number of unknowns in M_k is the number of edges of K.

Figure 4 shows the ellipses associated with the metrics M_k on a cut through a 150 thousand hexahedral element mesh. Indeed, the metric M_k can be written as $M_k = R^{-1}\Lambda R$ where the unit rotation matrix R and the stretching matrix Λ combine to transform the inscribed sphere inside a unit cube into the inscribed ellipse inside the hexahedron K. Note that for display purposes, the ellipse present $1/\sqrt{(\lambda_i)}$, since $\lambda_i = 1/h_i^2$ in equation 15.

In figure 3, the color used for the ellipses corresponds to the non-conformity measure presented in [25] that measures the degree to which M_k corresponds to M_s. This measure helps evaluate how much the mesh satisfies the metric and is presented in the next section.

NON-CONFORMITY COEFFICIENT

In a perfectly adapted mesh, we aim, for each element, that the current metric M_K be equal to the target metric derived from interpolation error estimation M_s, and we therefore seek

$$M_K = M_s.$$

The metric non-conformity residual $T_{NC,K}$ of an element measures the distance between the two metrics, with M_s the target metric averaged over the region covered by element K. In tensor form, one way of measuring this distance is as follows:

$$T_{NC,K} = M_s^{-1}M_K + M_K^{-1}M_s - 2I.$$

Taking a tensor norm yields the non-conformity measure $\mathscr{E}_K$ of element K.

$$\mathscr{E}_K = \|T_{NC,K}\| = \sqrt{\mathrm{tr}\left(\mathrm{T}_{\mathrm{NC,K}}^{\mathrm{T}}\mathrm{T}_{\mathrm{NC,K}}\right)}$$

Summing over all elements, we can define a metric non-conformity coefficient for the whole mesh as

$$\mathscr{E}_{\mathscr{T}_h} = \sum_K \mathscr{E}_K / N_K$$

where N_K is the number of elements in the mesh.

The value $\mathscr{E}_{\mathscr{T}_h}$ ranges form 0 for a perfectly adapted mesh to infinity for a mesh comprising degenerate elements. This definition may be approximated when using non-simplicial elements by decomposing elements into their corner sub-simplices and averaging sub-simplices $\mathscr{E}_K$ non-conformity coefficients [26].

$$\overline{M_K} = \overline{M_s}$$

with

$$\overline{M_s} = \int_K M_s(\vec{x})dK \Big/ \int_K dK$$

The computation of $\overline{M_K}$ must be made sensitive to all types of element degeneracies by making sure that the non-conformity coefficient $\mathscr{E}_K$ become infinite when a sub-simplex degenerates.

Visualizing the principal mesh modifications required by the estimator

The error estimator yields a target metric for element K that can be compared with the metric K using the non conformity measure. This measure can be rewritten so as to display information on the main refinement operations to perform to the mesh and the main coarsening operations to perform to the mesh.

Indeed, we can write:

$$r_b = M_s^{-1} M_k - I \tag{18}$$
$$r_s = M_k^{-1} M_s - I \tag{19}$$

from which we obtain that $T_{NC,K} = r_b + r_s$. As the size of an element K decreases, the metric of the element M_k increases and r_b increases. Conversely, as the size of an element increases, M_k^{-1} increases and r_s increases. So r_b can be seen as a residue sensible to elements that are too big, and r_s can be seen as a residue that is sensible to elements that are too small.

The matrices r_a and r_b are neither symmetric nor positive definite. A singular value decomposition can be used to determine the directions and the amplitude of modifications required on the mesh.

$$svd(r_s) = U_s S_s V_s^t$$

where U_s and V_s are rotation matrices and S_s contains the eigenvalues of the decomposition. If no modifications are required in a particular direction, the rank deficiency will be elegantly noticed and solved by the SVD decomposition by setting the corresponding eigenvalue to zero. The same decomposition can be applied to r_b. The SVD decomposition generates a set of positive eigenvalue sorted in descending order. This means that the first eigenvector of U is the direction in which the residue is strongest. In order to visualize the principal mesh modification actions that the anisotropic error estimator wants to perform on the mesh, we can therefore display the eigenvectors of U^t. Furthermore, by scaling these vectors by the eigenvalues S.

In figure 5, the green lines show the principal direction of the refinement operation and the length of the vector is related to how much this operation is required. The red vectors show the principal direction in which the mesh needs to be coarsened.

ACKNOWLEDGMENT

Thanks go to Maryse Page for her help on the conical diffuser test case and to Marie-Gabrielle Vallet and Julien Dompierre for their help on metrics and adaptivity.

REFERENCES

[1] Leibovich, S., 1978. "The structure of vortex breakdown". *Annual Review of Fluid Mechanics,* ***10***(1), pp. 221–246.

[2] Escudier, M., 1987. "Confined vortices in flow machinery". *Annual Review of Fluid Mechanics,* ***19***(1), pp. 27–52.

[3] Alekseenko, S. V., Kuibin, P. A., Okulov, V. L., and Shtork, S. I., 1999. "Helical vortices in swirl flow". *Journal of Fluid Mechanics,* ***382***(1), pp. 195–243.

[4] Shtern, V., and Hussain, F., 1999. "Collapse, symmetry breaking, and hysteresis in swirling flows". *Annual Review of Fluid Mechanics,* ***31***(1), pp. 537–566.

[5] Shtern, V., and Hussain, F., 2003. "Effect of deceleration on jet instability". *Journal of Fluid Mechanics,* ***480***, pp. 283–309.

[6] Ciocan, G. D., Iliescu, M. S., Vu, T. C., Nennemann, B., and Avellan, F., 2007. "Experimental study and numerical simulation of the flindt draft tube rotating vortex". *Journal of Fluids Engineering,* ***129***(2), p. 146158.

[7] Alauzet, F., 2008. "High-order methods and mesh adaptation for euler equations". *International Journal for Numerical Methods in Fluids,* ***56***(8), pp. 1069–1076.

[8] Bottasso, C. L., 2004. "Anisotropic mesh adaption by metric-driven optimization". *International Journal for Numerical Methods in Engineering,* ***60***(3), pp. 597–639.

[9] Bourgault, Y., Picasso, M., Alauzet, F., and Loseille, A., 2009. "On the use of anisotropic a posteriori error estimators for the adaptative solution of 3d inviscid compressible flows". *International Journal for Numerical Methods in Fluids,* ***59***(1), pp. 47–74.

[10] Joubarne, ., Guibault, F., Avellan, F., and Braun, O., in press. "Wing tip vortex capture by anisotropic mesh adaptation". *International Journal for Numerical Methods in Fluids*.

[11] Clausen, P. D., Koh, S. G., and Wood, D. H., 1993. "Measurements of a swirling turbulent boundary layer developing in a conical diffuser". *Experrimental Thermal and Fluid Science,* ***6***(1), pp. 39–48.

[12] Clausen, P., and Wood, D., 1987. "Some measurements of swirling flow through an axisymmetric diffuser". In Proceedings of Sixth Symposium on Turbulent Shear Flows, Paul Sabatier University, Toulouse, France.

[13] Page, M., Giroux, A.-M., and B.Massé, 1996. "Turbulent swirling flow computation in a conical diffuser with two commercial codes". In Proceedings of CFD'96, Fourth Annual Conference of the CFD Society of Canada, Ottawa, Canada.

[14] Page, M., Giroux, A.-M., and B.Massé, 1997. "Turbulent swirling flow computations in a conical diffuser". In Proceedings of the FIDAP User's Meeting, Burlington, USA.

[15] Gyllenram, W., and Nilsson, H., 2006. "Very large eddy simulation of draft tube flow". In Proceedings of the 23rd IAHR Symposium on Hydraulic Machinery and Systems.
[16] Nilsson, H., Page, M., Beaudoin, M., Gschaider, B., and Jasak, H., 2008. "The OpenFOAM turbomachinery working group, and conclusions from the turbomachinery session of the third OpenFOAM workshop". In Proceedings of the 24th IAHR Symposium on Hydraulic Machinery and Systems.
[17] Bounos, O., 2008. Studies of the ercoftac conical diffuser using openfoam. Tech. rep., Chalmers University of Technology, Department of Applied Mechanics. Presented at the 3rd OpenFOAM Workshop, Milan, Italy.
[18] ANSYS Inc., 2009. *ANSYS CFX-Solver Theory Guide*.
[19] Wilcox, D. C., 1993. *Turbulence Modeling for CFD*. DCW Industries, Inc.
[20] Frey, P. J., and Alauzet, F., 2005. "Anisotropic mesh adaptation for cfd computations". *Computer Methods in Applied Mechanics and Engineering*, ***194***(48-49), pp. 5068–5082. doi: DOI: 10.1016/j.cma.2004.11.025.
[21] Alauzet, F., Li, X., Seol, E., and Shephard, M., 2006. "Parallel anisotropic 3d mesh adaptation by mesh modification". *Engineering with Computers*, ***21***(3), pp. 247–258.
[22] Dompierre, J., Vallet, M.-G., Bourgault, Y., Fortin, M., and Habashi, W. G., 2002. "Anisotropic mesh adaptation: towards user-independent, mesh-independent and solver-independent cfd. part iii. unstructured meshes". *International Journal for Numerical Methods in Fluids*, ***39***(8), pp. 675–702.
[23] Castro-Daz, M. J., Hecht, F., Mohammadi, B., and Pironneau, O., 1997. "Anisotropic unstructured mesh adaption for flow simulations". *International Journal for Numerical Methods in Fluids*, ***25***(4), pp. 475–491.
[24] Zienkiewicz, O. C., Zhu, J. Z., and Wu, J., 1993. "Superconvergent patch recovery techniques - some further tests". *Communications in Numerical Methods in Engineering*, ***9***(3), pp. 251–258.
[25] Labbé, P., Dompierre, J., Vallet, M.-G., Guibault, F., and Trépanier, J. Y., 2004. "A universal measure of the conformity of a mesh with respect to an anisotropic metric field". *International Journal for Numerical Methods in Engineering*, ***61***(15), pp. 2675–2695.
[26] Sirois, Y., Dompierre, J., Vallet, M.-G., and Guibault, F., 2005. "Measuring the conformity of non-simplicial elements to an anisotropic metric field". *International Journal for Numerical Methods in Engineering*, ***64***(14), pp. 1944–1958.

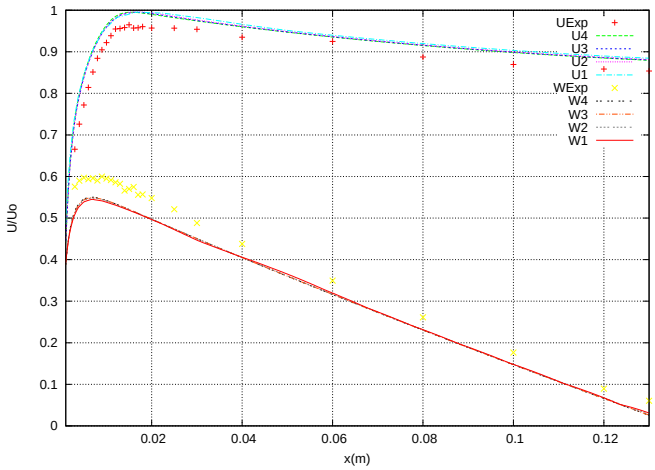

(a) x=25mm

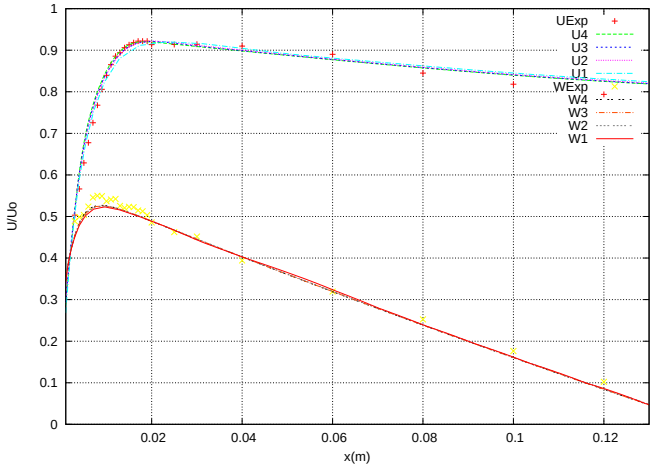

(b) x=60mm

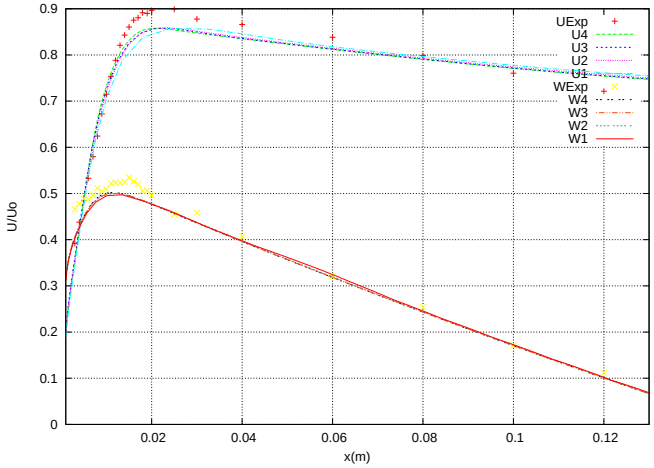

(c) x=100mm

FIGURE 2. Longitudinal component of the velocity

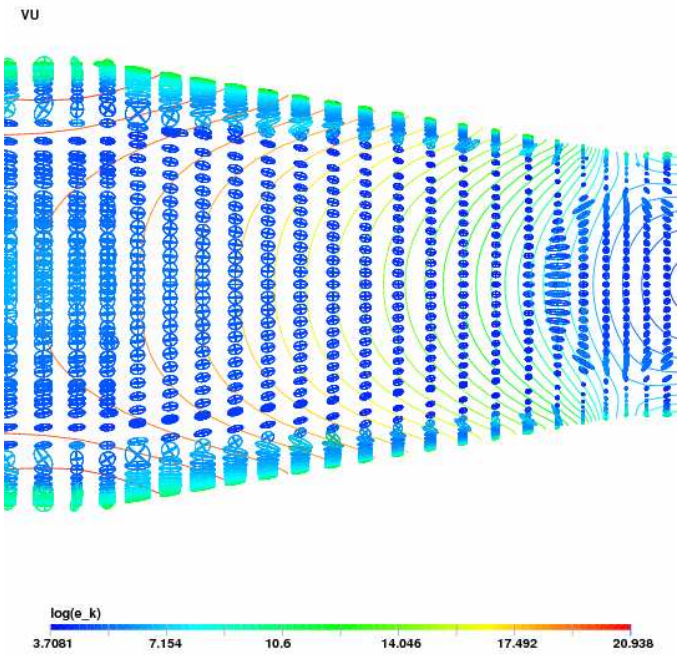

FIGURE 3. ELLIPSES REPRESENTING M_s ON A CUT PLANE.

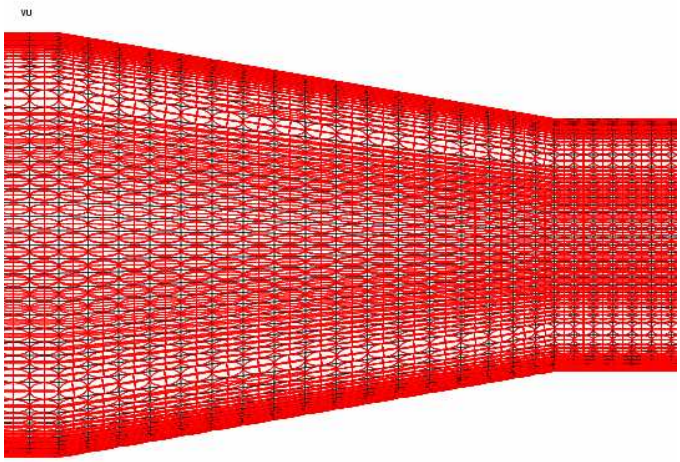

FIGURE 4. ELLIPSES REPRESENTING M_k ON A CUT PLANE.

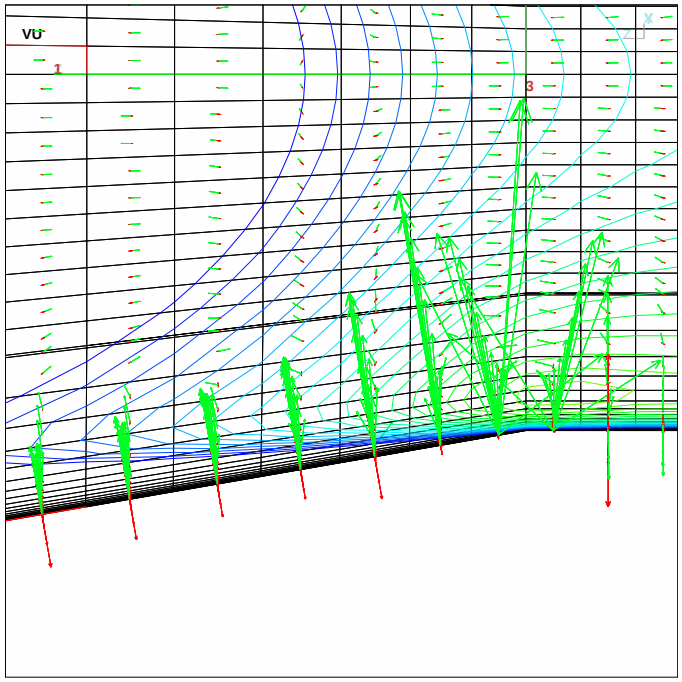

FIGURE 5. Principal modifications to the mesh according to speed estimator.

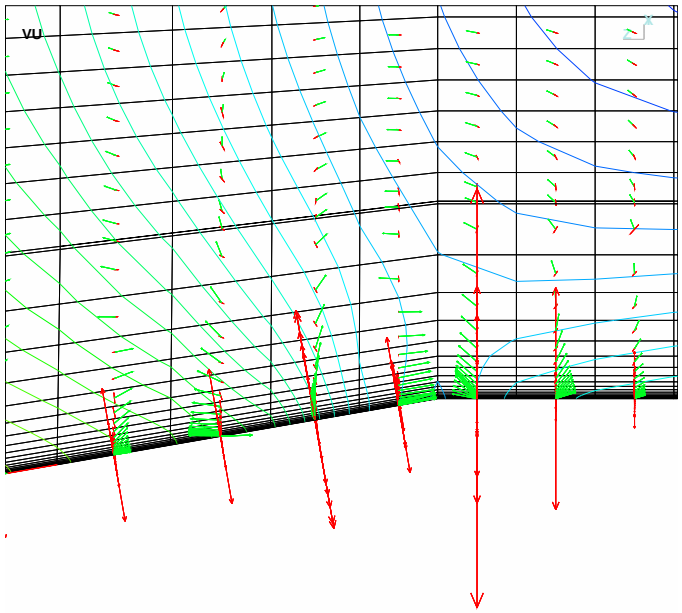

FIGURE 6. Principal modifications to the mesh according to pressure estimator.